Nanoscale Advances

ROYAL SOCIETY OF CHEMISTRY

PAPER

View Article Online
View Journal | View Issue

Open Access Article. Published on 25 2021. Downloaded on 2025/8/4 10:27:00.
This article is licensed under a Creative Commons Attribution-NonCommercial 3.0 Unported Licence.

Check for updates

Cite this: *Nanoscale Adv.*, 2021, **3**, 6974

Ultrasensitive two-dimensional material-based MCF-7 cancer cell sensor driven by perturbation processes†

Sophia S. Y. Chan,[a] Denise Lee,[a] Maria Prisca Meivita,[a] Lunna Li,[a] Yaw Sing Tan,[b] Natasa Bajalovic *[a] and Desmond K. Loke *[ac]

Received 9th August 2021
Accepted 13th October 2021

DOI: 10.1039/d1na00614b

rsc.li/nanoscale-advances

Changes in lipid composition and structure during cell development can be markers for cell apoptosis or various diseases such as cancer. Although traditional fluorescence techniques utilising molecular probes have been studied, these methods are limited in studying these micro-changes as they require complex probe preparation and cannot be reused, making cell monitoring and detection challenging. Here, we developed a direct current (DC) resistance sensor based on two-dimensional (2D) molybdenum disulfide (MoS_2) nanosheets to enable cancer cell-specific detection dependent on micro-changes in the cancer cell membrane. Atomistic molecular dynamics (MD) simulations were used to study the interaction between 2D MoS_2 and cancer lipid bilayer systems, and revealed that previously unconsidered perturbations in the lipid bilayer can cause an increase in resistance. Under an applied DC sweep, we observed an increase in resistance when cancer cells were incubated with the nanosheets. Furthermore, a correlation was observed between the resistance and breast cancer epithelial cell (MCF-7) population, illustrating a cell population-dependent sensitivity of our method. Our method has a detection limit of $\sim 3 \times 10^3$ cells, below a baseline of $\sim 1 \times 10^4$ cells for the current state-of-the-art electrical-based biosensors using an adherent monolayer with homogenous cells. This combination of a unique 2D material and electrical resistance framework represents a promising approach for the early detection of cancerous cells and to reduce the risk of post-surgery cancer recurrence.

Introduction

Biomarkers are quintessential in healthcare to support the management of infectious diseases (recent examples include the use of antibodies and nucleic acids as biomarkers for Covid-19 tests),[1] and to determine the severity and outcome of life-threatening diseases such as cancer. As one of the leading causes of death worldwide, cancer accounts for more than 9 million deaths per year with cases on the rise.[2] Moreover, cancer is currently the leading cause of death in Singapore, accounting for approximately 28% of mortality in 2019.[3] In particular, there is a need to discover a biomarker that can be used to detect diseases where early diagnosis is crucial or currently difficult. Changes in cell membrane components (*e.g.* lipids and proteins) are emerging as an ideal candidate for applications in diagnosis and treatment; for example, changes in lipid composition during cancer cell development can lead to carcinogenesis and metastasis.[4,5] Detecting these cancer cell membrane-specific changes with high sensitivity is of vital significance in cancer treatments: for early cancer diagnosis to improve patient outcome, and to reduce the risk of cancer recurrence after cancer treatment.[6,7]

Each cell type possesses a unique cell membrane composition, comprising a variety of phospholipids that form a bilayer, with embedded proteins.[5,8,9] Phospholipids generally have a polar head group and a long, hydrophobic tail. Polar hydrophilic heads point outwards and are in contact with the aqueous fluids inside (cytoplasm) and outside (extracellular medium) the cell. On the other hand, the non-polar hydrophobic tails point inwards, and are not in contact with the aqueous phase inside and outside the cells. Typical phospholipid components found in the cell membrane are phosphatidylcholine (PC), phosphatidylserine (PS), phosphatidylethanolamine (PE), sphingolipid (SL) and cholesterol. The cell membrane is crucial for cell signalling and regulating cell processes (endocytosis, enzymatic activity, transport *etc.*), as well as its structural function.[5,10] Normal cells have an asymmetric lipid bilayer, where the composition of the inner and outer layer, or leaflet are not the same.[5,9] A loss in asymmetry can be associated with apoptosis or diseases such as cancer.[5,11,12] Non-asymmetric

[a]*Department of Science, Mathematics and Technology, Singapore University of Technology and Design, Singapore 487372, Singapore. E-mail: natasa_bajalovic@sutd.edu.sg; desmond_loke@sutd.edu.sg*

[b]*Bioinformatics Institute, Agency for Science, Technology and Research (A*STAR), Singapore 138671, Singapore*

[c]*Office of Innovation, Changi General Hospital, Singapore, 529889, Singapore*

† Electronic supplementary information (ESI) available: Simulation results and other experimental data. See DOI: 10.1039/d1na00614b

© 2021 The Author(s). Published by the Royal Society of Chemistry

Open Access Article. Published on 25 2021. Downloaded on 2025/8/4 10:27:00.
This article is licensed under a Creative Commons Attribution-NonCommercial 3.0 Unported Licence.

cancer cell membranes tend to have different cell membrane potentials due to an increase in charged lipids (*e.g.* PS and PE) found in the outer leaflet.[11,13,14] Changes in lipid asymmetry and composition contribute to the overall cancer cell membrane potential,[15,16] and can be used to understand cellular mechanisms,[17,18] or as biomarkers for cancer progression and detection,[10,19,20] and targeted cancer-cell treatments.[11,14]

There are three different types of cell membrane potential: surface, transmembrane and dipole potential. The surface potential (Ψ_s) describes the accumulation of charges at the interface between the cell membrane and the extracellular media, while the transmembrane potential ($\Delta\Psi$) describes the difference in potential across the membrane. Cell membranes also have a dipole potential (Ψ_d), which defines the orientation of lipid dipolar residues (hydrophobic lipid tails) and extracellular water molecules.[18,21,22] Surrounding water molecules, phospholipid heads and hydrophobic tails can contribute to changes in Ψ_d for cancer cell membranes due to the different lipid compositions and packing density.[13,23–25] Changes in Ψ_d were also observed after lipid bilayer perturbation.[26] Although lipid bilayer composition and disruption have been characterised *via* traditional fluorescent methods, they can be problematic because they tend to be indirect, or require additional steps for substrate preparation and usually cannot be reused.

Electrical-based techniques are advantageous and promising candidates for understanding perturbations in the cell membrane by investigating the changes in native bioelectrical signals.[27–29] However, using traditional direct current (DC) or alternating current (AC) electrical stimulation to detect cancer cell types remains challenging due to poor sensitivity (a high limit of detection of several ten thousand cells). Advanced materials with unique electrical properties can improve the performance of the electrical-based devices.[30,31] Recently, two dimensional (2D) materials have been used for cancer cell detection, including, graphene-based materials[32,33] and transition metal dichalcogenides (TMDs).[34,35] For example, devices based on functionalised graphene oxide have demonstrated high sensitivity for detecting circulating tumor cells (CTCs).[36] In addition, a 2D graphite-like carbon nitride nanosheet-based electrode was used to detect cervical cancer cells (HeLa) in suspension with a low limit of detection. However, some of these nanomaterials suffer from long-term toxicity.[37] Identifying an appropriate 2D material with a strong affinity for specific biomarkers, native biocompatibility and unique electrical properties is critical for developing a sensitive electrical-based cell detector.

Molybdenum disulfide (MoS_2) is a TMD with unique physical, chemical, electrical and optical properties on a 2D scale.[38,39] As the MoS_2 thickness is reduced, the material transits from an indirect band gap in the bulk to a semiconductor with a direct band gap. MoS_2 nanosheets are biocompatible,[40,41] have a similar conductivity to cancer cells[20] and are currently harnessed in biological applications such as cancer therapeutics (*e.g.* drug delivery and photothermal therapy),[42–45] tissue engineering[46,47] and biosensors[20,48,49] and other applications. Although the electrical properties of MoS_2 nanomaterials have been investigated, studies concerning the interaction between cancer cell membranes and MoS_2, and its application in DC resistance sensing are limited.

Here, we explored the interactions between a cancer cell membrane and MoS_2 nanosheet using atomistic molecular dynamics (MD) simulations. Our calculations demonstrated a previously unconsidered decrease in the Ψ_d after MoS_2 interaction. We hypothesise that the decrease in Ψ_d is due to the lipid bilayer disruption and the final configuration of MoS_2 within the lipid bilayer. Motivated by this theoretical finding, we developed an electrical resistance-based system using MoS_2 and demonstrated a marked increase in resistance when epithelial breast cancer cells (MCF-7) were incubated with MoS_2 nanosheets. Our experiments agreed well with our hypothesis: the addition of MoS_2 nanosheets increased the resistance of the medium cell population. Furthermore, a correlation was observed between resistance and MCF-7 cell population, illustrating a cell population-dependent sensitivity of our method. We also demonstrate a limit of detection of $\sim 3 \times 10^3$ cells, lower than the baseline of $\sim 1 \times 10^4$ cells for current state-of-the-art electrical-based methods using adherent monolayer of homogenous cells, which allows for the detection of cells at low levels for clinically relevant cancer diagnosis and treatment. In addition, our system preparation uses time-saving few steps and all the components can be reused compared to traditional time-consuming multi-step detection systems, allowing for a rapid diagnosis while saving cost. This proposed combination of a unique 2D material and electrical resistance framework is a promising method for the development of lab-on-chip platforms for clinical purposes.

Experimental

Simulation parameterisation

MoS_2 sheet was prepared as previously described.[50] A 4.1 nm × 4.2 nm single-layer MoS_2 sheet with two zig-zag edges, one terminating with S atoms and the other with Mo atoms, and two armchair edges was generated using Materials Studio. Bonded force field parameters were provided by Varshney *et al.*,[51] while non-bonded force field parameters were provided by Luan and Zhou[52] (see ESI Table S2†). Potential energy contributions from bond angles larger than 82° in the MoS_2 sheet were not considered.

A model lipid bilayer system representing the cell membrane of a cancer cell was generated using CHARMM-GUI.[53,54] The lipid bilayer system was composed of neutral dipalmitoylphosphatidylcholine (DOPC) and negatively charged dipalmitoylphosphatidylserine (DOPS) lipids (composition found in ESI Table S3†). There were 242 lipids in total, 121 in each leaflet, and the system was solvated in a solution with 40 TIP3P water molecules per lipid and 0.15 M NaCl.[55] The system was equilibrated for 50 ns before monolayer MoS_2 was added in subsequent simulation runs.

Simulation details

Atomistic MD simulations were performed with GROMACS 5.0.4 using the Slipids force field as described before.[50,55–57] Initially, the MoS_2 nanosheet was positioned parallel with and ~2.5 nm above the lipid bilayer. The simulation box, with

Open Access Article. Published on 25 2021. Downloaded on 2025/8/4 10:27:00.
This article is licensed under a Creative Commons Attribution-NonCommercial 3.0 Unported Licence.

dimensions of 8.72 nm × 8.86 nm × 10.50 nm, was filled with 1341 TIP3P water molecules,[58] 0.15 NaCl, and 52 sodium counterions. The system was energy minimised using the steepest descent algorithm for up to 2000 steps, and then equilibrated in the isochoric–isothermal (*NVT*) ensemble for $t =$ 100 ps. The temperature of the system was maintained at $T =$ 300 K using the velocity-rescaling thermostat[59] with a coupling constant of 0.5 ps. Another equilibration step was performed in the isothermal–isobaric (*NPT*) ensemble for $t = 100$ ps, followed by the production run for 700 ns. The pressure was kept constant by the Parrinello–Rahman barostat at $P = 1$ bar,[60] with a semi-isotropic pressure coupling scheme while the temperature was kept constant using the Nosé–Hoover thermostat.[61,62] Two independent MD simulation runs with different initial atomic velocities were performed. Long-range electrostatic interactions were treated with the particle-mesh Ewald scheme,[63,64] and van der Waals interactions were calculated with a cut-off distance of 1 nm. All lipid and MoS_2 bonds were constrained using the LINCS algorithm. A time step of $t = 2$ fs was used with a leapfrog integrator and coordinates of all atoms were saved every 20 ps.

Data analysis

Interaction energies between the MoS_2 and the lipid bilayer were extracted from the simulation using the Gromacs tool *gmx energy*. They were obtained as Lennard-Jones potentials, which are van der Waals interactions.

Using the Gromacs tool *gmx mindist*, atom count was calculated for the number of lipid atoms close to the MoS_2 nanosheet. The total atom count describes the total number of lipid atoms that are less than 6 Å away from the MoS_2 nanosheet at any time during the simulation run.

Transmembrane dipole potential (Ψ_d) was calculated using the Gromacs tool *gmx potential*. The potential was calculated from the charge density, which was obtained from one hundred slice profiles along the *x*–*y* plane. The thickness of each slice was ~0.92 Å. The dipole potential was obtained by double integration of charge density using the following equation:[13,25]

$$\Psi_d = -\frac{1}{\varepsilon_0}\int_0^z \int_0^{z'} \rho(z'')\mathrm{d}z''\mathrm{d}z' \quad (1)$$

where ε_0 is the electrostatic permittivity in vacuum, $\rho(z)$ is the charge density and z is the position along the z-axis. Ψ_d for the lipid bilayer was calculated for the entire membrane-only simulation and the last 100 ns of the membrane with MoS_2 simulation run.

The angle of the MoS_2 nanosheet relative to the lipid bilayer's *x*–*y* plane was calculated for every frame of the trajectory using the Gromacs tool *gmx bundle*. The angle was between the nanosheet and *z*-axis was measured for every frame (20 ps) during the trajectory, and it was then translated to the lipid bilayer axis by 90°.

TMD preparation

Few layer MoS_2 sheets in deionised water (2D Semiconductors) were sonicated (Elmasonic P) for ~10 min at room temperature (RT) before material characterisation and incubation. MoS_2 was drop casted on silicon (Si) substrate prior to the Raman spectroscopy and scanning electron microscopy (SEM). The chemical composition of the 2D MoS_2 sheets were analysed by energy-dispersive X-ray spectroscopy (EDS) point analysis: the EDS analysis indicated the stoichiometric ratio of Mo : S to be about 1 : 2.

Cell culture

Breast cancer cell line MCF-7 were cultured in Dulbecco's Modified Eagle Media (DMEM) (Nacalai Tesque) containing 7% fetal bovine serum (FBS) and 5 mM of L-glutamine (Gibco), maintained in a 5% CO_2 environment at 37 °C. Cells were observed using an inverted light microscope with a 10× objective lens (Olympus DP22).

Electrical characterisation

MCF-7 cells (3×10^3 cells) were seeded in our setup 24 h prior to material addition; ITO electrodes deposited on a glass substrate (LaTech) with a cloning cylinder (Sigma) adhered with silicone adhesive (Fig. 2a). After incubating the material with the cells for an additional 24 h, current–voltage (*I*–*V*) sweeps ($V = 0$ V to -5 V, dual sweep) were performed using the semiconductor characterisation system (Keithly 4200-SCS). The resistance (R) was calculated for all the voltage points using the following equation:

$$R = \frac{V}{I} \quad (2)$$

where I is the measured current (A) and V is the applied voltage (V). The resistance was averaged between $V = -1.7$ V to -5 V in the forward direction and $V = -5$ V to -3.2 V in the backward direction. For cell population testing, MCF-7 cells were plated at $n = 3 \times 10^3$, 4×10^3 and 5×10^3 cells in our setup. Cells were then subjected to the same material addition and electrical pulses.

Cell viability assay

To investigate MoS_2 cytotoxicity, MCF-7 cells were plated in 96-well plates and cultured ~24 h prior to treatment. Sonicated MoS_2 nanosheets were added at a concentration ranging from 0–100 μM at 25 μM increments for $t = 24$ h and 48 h. Cell viability and cytotoxic effects of MoS_2 nanosheets were determined using a WST-1 assay. After adding 10% WST-1 (Sigma) in media, the cells were incubated for ~4 h at 37 °C. Cell viability was estimated by measuring absorbance at $\lambda = 450$ nm. Cell viability was also tested ~24 h after applying the DC sweep.

Results & discussion

We performed atomistic molecular dynamic (MD) simulations to understand the interaction between the cancer lipid bilayer system and a MoS_2 nanosheet. Two simulation runs were performed for 700 ns each, and we observed similar interactions between MoS_2 and the lipid bilayer for both runs. Fig. 1 shows representative data obtained from one of the two simulation

 © 2021 The Author(s). Published by the Royal Society of Chemistry

Open Access Article. Published on 25 2021. Downloaded on 2025/8/4 10:27:00.
This article is licensed under a Creative Commons Attribution-NonCommercial 3.0 Unported Licence.

runs. Our model lipid bilayer for the cell membrane of a cancer cell is a simplified version of that modelled by Klähn and Zacharias,[65] wherein the outer lipid layer contains an increased proportion of phosphatidylserine (PS) compared to that of a healthy cell (lipid composition can be found in ESI Table S2†).

Fig. 1a shows the snapshots of the simulation with time. The first point of contact is between a corner of the MoS_2 nanosheet and the upper leaflet of the lipid bilayer (~6 ns). The nanosheet then tilts towards the lipid bilayer, aligning itself parallel to the lipid bilayer at around 50 ns. At ~400 ns, the nanosheet is tilted, and phospholipids are extracted onto the sulphur (S) side facing the lipid bilayer (phospholipid extraction). Moreover, the lipid bilayer appears to curve below the MoS_2 nanosheet, suggesting the disruption of the lipid bilayer. The same corner is in contact with the lipid bilayer during the entire simulation. We also calculated the changes in atom count (the number of lipid atoms less than 6 Å away from the MoS_2 nanosheet) and van der Waals (vdW) interaction energy (Fig. S1a†). Two significant changes were observed for atom count and vdW energy: one around 50 ns and the other at around 400 ns, which correspond to the nanosheet laying parallel to the upper leaflet of the lipid bilayer and the tilting of the nanosheet on the lipid bilayer respectively (Fig. S1a†). The center of mass (CoM) distance was also calculated between the nanosheet and the upper leaflet of the lipid bilayer (Fig. S1b†). After the initial contact, CoM was generally consistent during the simulation.

We calculated the dipole potential (Ψ_d) of the cancer lipid bilayer system before and after MoS_2 interaction (Fig. 1b and c). Without MoS_2, the system has a Ψ_d profile that is typical of a pure lipid bilayer system, consistent with literature (Fig. 1b).[13,25] Using a reference value of 0 V for the aqueous phase, the profile showed a sharp increase in Ψ_d across the lipid head region with a peak value of ~0.47 V. These peaks were located ~1.28 nm ($Z = \pm 1.28$ nm) above and below the bilayer center ($Z = 0$ nm), corresponding to the top part of the lipid tails near the lipid head groups. The local minima, typically associated with the unsaturated double bonds along the lipid tails, were observed ~0.8 nm ($Z = \pm 0.8$ nm) above and below the bilayer center. A global maximum of ~0.63 V was reached at $Z = 0$ nm, which can be attributed to the presence of partial changes and corresponding dipoles at the terminal methyl groups on the lipid tails. After MoS_2 interaction, the Ψ_d profile of the lipid bilayer system becomes asymmetric (Fig. 1c): the Ψ_d profile broadens, the global maximum decreases (~0.51 V) and the peak shifts downwards from $z = 0$ nm to -1.5 nm (Fig. 1b–d). This could be due to lipid bilayer perturbation, where the curvature of the lipid bilayer induced by the MoS_2 nanosheet can result in the majority of the terminal methyl groups shifting away from the bilayer center. There is a new peak located at ~1.4 nm above from the bilayer center ($Z = +1.4$ nm), which could be associated with phospholipid extraction as some of the lipids shift away from the bilayer center towards the material. Moreover, the angle of MoS_2 relative to the lipid bilayer (x–y) plane was calculated for the duration of the simulation (Fig. 1e). As observed in Fig. 1a, the MoS_2 nanosheet aligns almost parallel (~4.7°) to the lipid bilayer before tilting towards the end of the simulation (~17.4°) (Fig. 1e). The vdW interactions between the MoS_2 nanosheet perturbed the lipid bilayer and resulted in bilayer curvature and phospholipid extraction (Fig. 1a–c), causing the changes in the Ψ_d profile, and could be considered as added resistance to the system (interlayer resistance).[66–68] This is because current prefers to flow laterally through the material (along the nanosheet).[66] To enhance the current flow, the ideal orientation of MoS_2 is parallel to the cell membrane. As a result, it is likely that the current is impeded by the perturbation of the lipid bilayer and tilted orientation of the MoS_2 nanosheet relative to the lipid bilayer.

We adopted an MoS_2-based DC resistance system to detect a medium population of MCF-7 cells based on micro-changes in the cell membrane. Our system comprises of two 650 nm-thick indium tin oxide (ITO) left and right electrodes deposited on a glass substrate, and a cloning cylinder was adhered to the electrodes using a silicone adhesive (Fig. 2a). The measured current is sensitive to the changes in Ψ_d due to the micro-changes in the cell membrane with the addition of the MoS_2 nanosheets. As embedded MoS_2 can perturb the lipid bilayer and affect Ψ_d, MCF-7 cells can be detected based on the changes in the resistance in the presence of the nanosheets.

Before interacting with the cells, 2D MoS_2 nanosheets were obtained by liquid-phase sonication to break the vdW forces between the layers. Each MoS_2 nanosheet consists of a few hexagonal S–Mo–S sheets (Fig. 2b) held together *via* vdW interactions. The structure and morphology of the sonicated samples were investigated. The nanosheets were well dispersed within the solution as observed by the typical red beam through the sonicated MoS_2 solution under irradiated light (Faraday–Tyndall effect) (Fig. 2b). MoS_2 flakes were drop casted on a silicon (Si) substrate prior to material characterisation. The Raman spectra (Fig. 2c) shows two characteristic Raman vibrational modes of the few-layered MoS_2, labelled E^1_{2g} at ~384.80 cm^{-1} and A_{1g} at ~405.46 cm^{-1}, similar to experimental data in literature.[69] The degenerate modes of E^1_{2g} symmetry correspond to the in-plane transversal and longitudinal vibrations of the sublayers in opposite directions, while the A_{1g} symmetry is a result of the third mode opposite-in-phase out-of-plane vibrations of the sublayers.[69] Fig. 2d shows a scanning electron microscope (SEM) image of the 2D MoS_2 flake, in which thin nanosheets were observed.

To investigate the interaction of the cell with MoS_2, we characterised the cytotoxicity of MoS_2 nanosheets for MCF-7 cells at different material concentrations and incubation times (Fig. 2e). Cell viability was determined using WST-1 cell proliferation assay (see Experimental section). After ~24 h, cell viability decreased with increasing material concentration. However, after ~48 h of incubation, cell viability was comparable to that of control (cells only). We concluded that, within our tested concentration range, the material is not cytotoxic to MCF-7 cells after ~48 h. To maximise our current output while maintaining cell viability, we chose a nanosheet concentration of 75 μM. MCF-7 cells were not significantly affected by MoS_2 at ~75 μM after 48 h (Fig. 2e), consistent with observations in previous studies.[41,70]

To study the micro-changes in the cell membrane as a result of MoS_2 interaction, we investigated the cell-dependent

Open Access Article. Published on 25 2021. Downloaded on 2025/8/4 10:27:00.
This article is licensed under a Creative Commons Attribution-NonCommercial 3.0 Unported Licence.

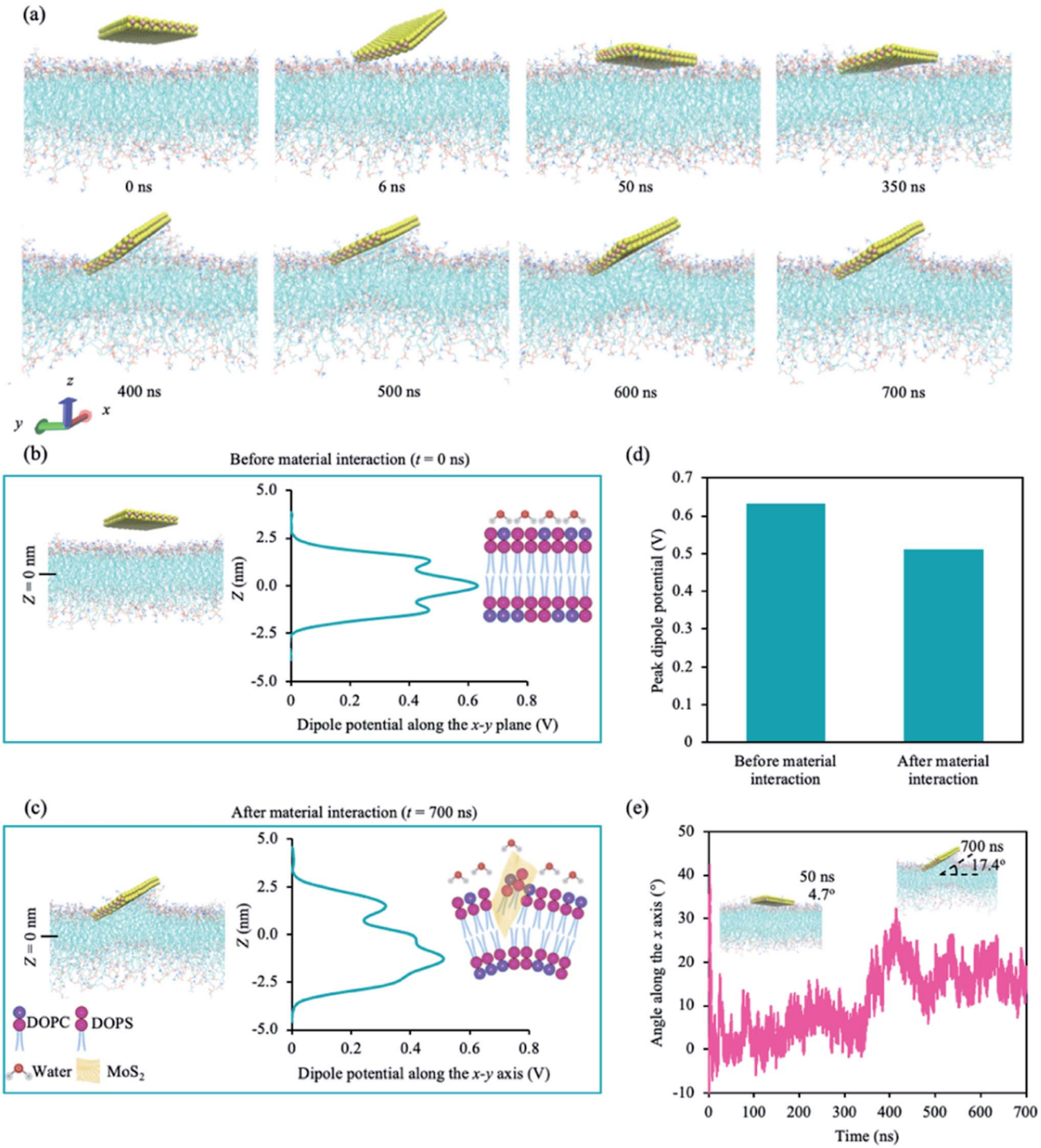

Fig. 1 Atomistic MD simulation of a MoS_2 nanosheet with a cancer lipid bilayer. (a) Snapshots of MoS_2 nanosheets interacting with cancer lipid bilayer with time. The MoS_2 nanosheet was positioned ~2.5 nm above the lipid bilayer. Colour coding of species as follows: S, yellow; Mo, pink; O, red; N, navy blue; C, aqua; P, gold. Waters are omitted for clarity. Dipole potential was calculated (b) before and (c) after MoS_2 interaction. Z (nm) represents the length of the simulation box along the z-axis. The schematic illustrations depict the changes in curvature of the phospholipids and phospholipid extraction around MoS_2 before and after material interaction, with water molecules on the extracellular surface. (d) Peak dipole potential (V) before and after material interaction for the cancer lipid bilayer systems. (e) Time evolution for the angle of MoS_2 relative to the lipid. The snapshot of the system at 50 ns and 700 ns are presented in the inset. The angles at 50 ns and 700 ns of the simulation were calculated to be ~4.7° and ~17.4°, respectively. Snapshots used in this figure follow the same axis. Data was taken from one simulation run as the interaction between MoS_2 and lipid bilayer were similar for two simulation runs.

 © 2021 The Author(s). Published by the Royal Society of Chemistry

Open Access Article. Published on 25 2021. Downloaded on 2025/8/4 10:27:00.
This article is licensed under a Creative Commons Attribution-NonCommercial 3.0 Unported Licence.

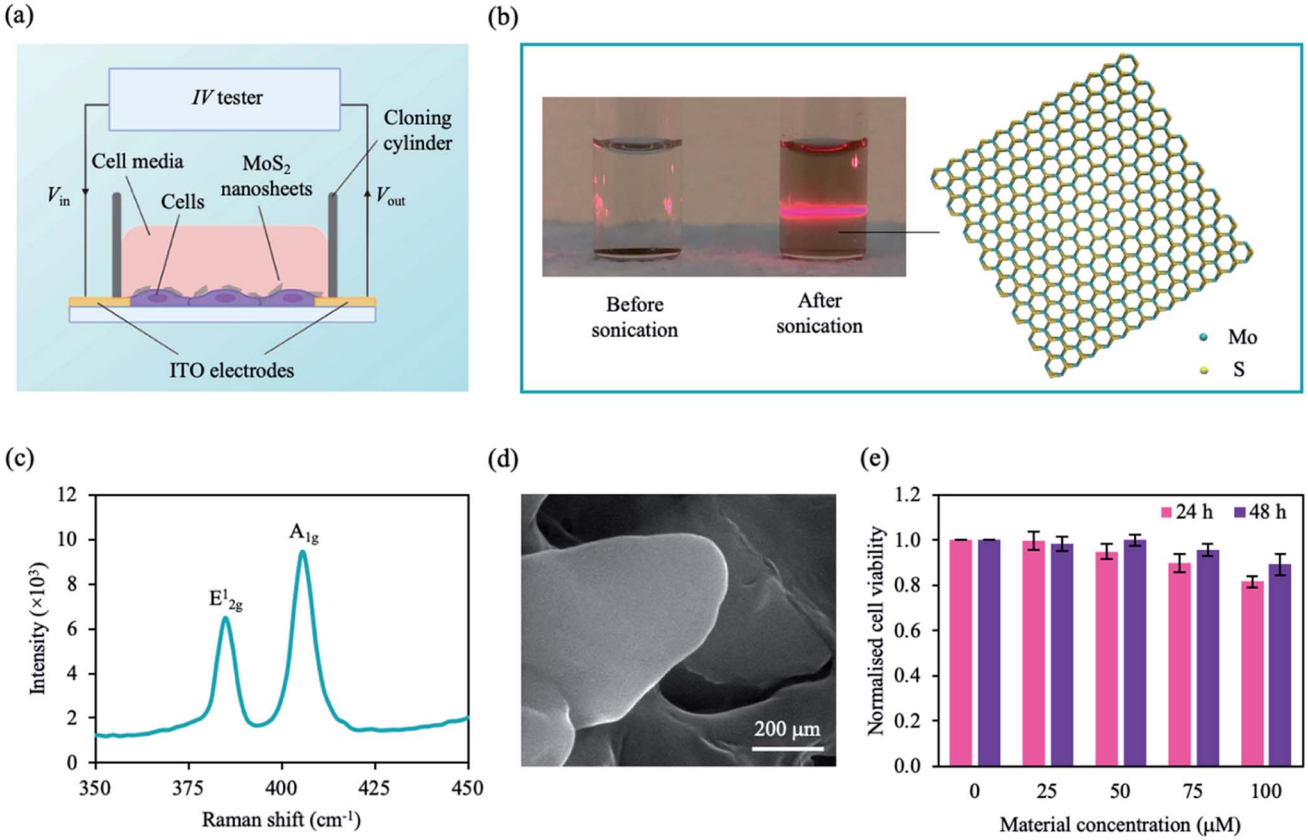

Fig. 2 Configuration of our system and MoS_2 characterisation. (a) A schematic of our setup. Cells were plated onto the ITO electrodes on a glass substrate and incubated with MoS_2 nanosheets. Using an IV tester, a DC sweep was applied and the cell signal was measured. (b) Photograph of MoS_2 solution before and after sonication (left panel). Upon laser irradiation, the Faraday–Tyndall effect was only observed for the sonicated MoS_2 solution as indicated by the strong red line through the solution. Schematic illustration of an MoS_2 nanosheet with a hexagonal S–Mo–S structure (right panel). Colour coding of species: S, yellow; Mo, cyan. (c) Raman spectra the MoS_2 nanosheet showing two vibrational modes. (d) Scanning electron microscope (SEM) image of MoS_2 nanosheets deposited on silicon (Si) substrate. (e) Normalised cell viability plotted as a function of MoS_2 concentration and incubation time (24 h, pink; 48 h, purple). Cell viability was estimated using a WST-1 assay with measured absorbance at $\lambda = 450$ nm. MCF-7 cells were grown in 96 well plates for ~24 h prior to treatment. Data represent mean ± SEM ($n = 6$ from 3 independent experiments). See ESI Table S1† for significance.

resistance of MCF-7 cells incubated with MoS_2 nanosheets (MCF-7/MS) and control (cells only) using a DC current–voltage (I–V) sweep with a negative voltage bias ($V = 0$ V to -5 V). The average resistance for MCF-7/MS was calculated using eqn (2) (see Experimental section), and normalised with control. Fig. 3a depicts a material-dependent increase in resistance obtained for MCF-7 cells. MCF-7/MS demonstrated an increase in normalised resistance compared to control (~9%, 3×10^3 cells), confirming the decrease in native Ψ_d as a result of adding MoS_2 nanosheets. Based on the results of our MD simulations, we speculate that the perturbation of the lipid bilayer system (resulting from the embedded MoS_2) and the final angle of the nanosheet contributed to the increase in resistance. Since current flows laterally (along the nanosheet) of the MoS_2, the tilt of the nanosheet disrupts the current flow along the cell membrane. Moreover, the extracted phospholipids could have increased the resistance between the nanosheet and the lipid bilayer, acting as an insulator and impeding current flow. Additionally, Fig. 3a shows the resistance for MCF-7/MS at different cell populations normalised to control of each cell population. After plating cells at different cell populations within our setup ($n = 3 \times 10^3$, 4×10^3 and 5×10^3 cells), we observed a significant increase in normalised resistance for MCF-7/MS plated at 4×10^3 and 5×10^3 cells. While it is expected that resistance should increase with cell population,[71–73] we observed no significant difference in normalised resistance across controls plated at different cell populations (3×10^3, 4×10^3 and 5×10^3 cells) (ESI Fig. S2†). On the other hand, the system showed a ~22% and ~28% increase in the normalised resistance when cell population was increased from 3×10^3 to 4×10^3 cells and 5×10^3 cells for MCF-7/MS, respectively. We determined the sensitivity of detection for our system by calculating the percentage change in normalised resistance between MCF-7/MS and control ($\Delta R_{\%}$)

$$\Delta R_{\%} = \frac{R_{\text{MCF-7/MS}} - R_{\text{MCF-7}}}{R_{\text{MCF-7}}} \times 100\% \quad (3)$$

where $R_{\text{MCF-7/MS}}$ and $R_{\text{MCF-7}}$ are the normalised resistances of MCF-7/MS and MCF-7, respectively (Fig. 3b). The reference resistance change for our system was calculated by the sum of

Open Access Article. Published on 25 2021. Downloaded on 2025/8/4 10:27:00.
This article is licensed under a Creative Commons Attribution-NonCommercial 3.0 Unported Licence.

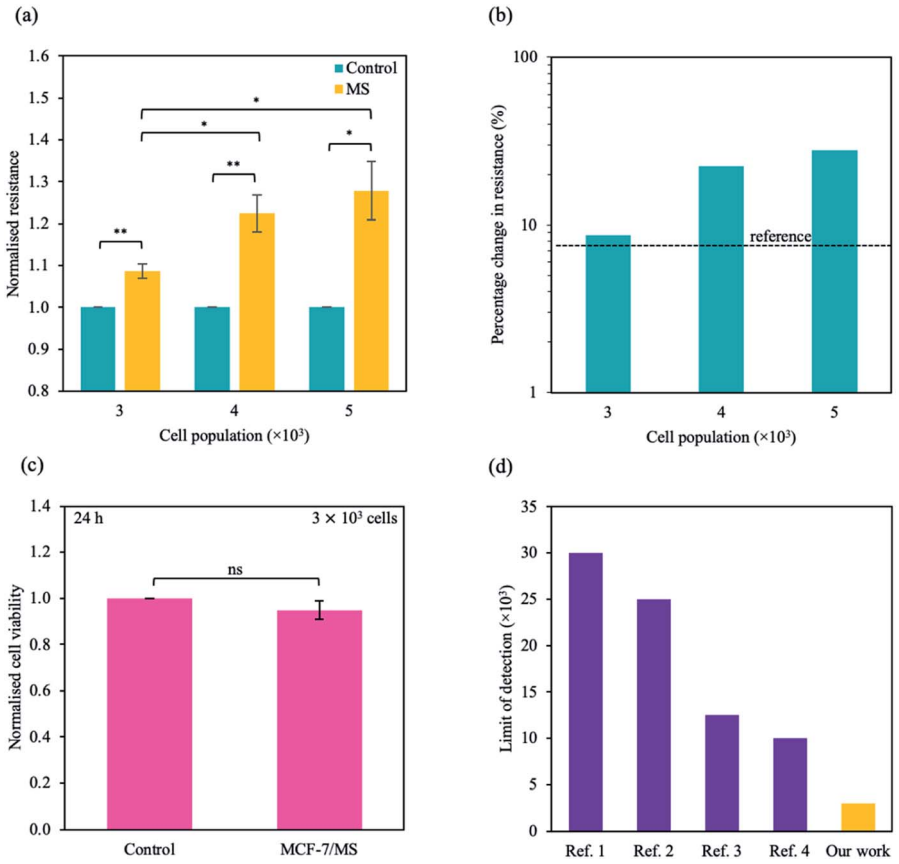

Fig. 3 Sensing micro-changes in the MCF-7 cell membrane using an MoS_2-based DC resistance sensor. (a) Normalised resistance for control (cells only) (green) and MCF-7/MS (yellow) plotted for various cell populations ($n = 3 \times 10^3$, 4×10^3 and 5×10^3 cells). The resistance was calculated from the DC sweep with a voltage bias of $V = 0$ to -5 V, and resistance values were normalised to its own control. (b) Semi-logarithmic plot of percentage change in normalised resistance for different cell populations. The black dotted line represents the reference resistance change (background signal + three times the standard deviation of the background signal (σ)). (c) Normalised cell viability plotted as a function of the presence of material. Cell viability was determined ~24 h after DC sweep using WST-1 assay measured at $\lambda = 450$ nm. (d) A plot of limit of detection for systems detecting adherent cells developed by other groups (purple) and this work presented here (yellow). Full references are available in ESI Table S4.† Data in (a) and (c) represent mean ± SEM ($n = 6$ from 3 independent experiments). Significance was calculated using a Student's t-test: non-significant (ns), $p < 0.05$ (*), $p < 0.01$ (**). For (a), unlabelled significance is denoted as ns.

the background signal plus three times the standard deviation (σ);[74,75] the background signal represents the change in resistance for media with MS (media/MS) normalised with media alone (ESI Fig. S3†). The detection limit for our system is $\sim 3 \times 10^3$ cells, estimated by the smallest cell population with a resistance change higher than the reference. It is likely that these sensitive changes in cell population were observed because of the micro-changes within the cancer cell membrane in the presence of MoS_2. Moreover, cell viability for a population of 3×10^3 cells was investigated after applying the DC sweep (Fig. 3c). From the WST-1 assay studies, the DC sweep did not affect cell viability after ~24 h for control or MCF-7/MS, indicating that our method has the potential for real-time, long-term cell monitoring. Using our method, we were able to detect MCF-7 cells with limit of detection of $\sim 3 \times 10^3$ cells, below a baseline of $\sim 1 \times 10^4$ cells for current state-of-the-art electrical-based biosensors with an adherent monolayer of homogenous cells (Fig. 3d). These findings demonstrate that our combination of 2D MoS_2 and DC resistance as a method to sense changes in the cancer cell membrane has the potential for detecting low levels of MCF-7 cells.

Due to the clinical importance of cell detection, numerous works have focused on developing an fluorescent-based method to detect various cell types (*e.g.* cancer cells, stem cells).[76–78] While there have been some promising research in detecting low numbers of cells in suspension, traditional fluorescent methods can require additional functionalisation, complex device preparation and additional time for result output.[79] Our work describes a few-step method to detect an adherent, single cell type without complex preparation methods, with a facile set up that can be combined with an electrical circuit. Here, we describe a method to detect an adherent monolayer of cancer cells using MoS_2-based DC resistance sensor. Using our method, we demonstrate a limit of detection of $\sim 3 \times 10^3$ cells, below the baseline of $\sim 1 \times 10^4$ cells for current state-of-the-art electrical-based biosensors with an adherent monolayer of homogenous cells.[80–83]

Alternative methods to traditional fluorescence detection such as electrochemical and electrical-based devices are

 © 2021 The Author(s). Published by the Royal Society of Chemistry

Open Access Article. Published on 25 2021. Downloaded on 2025/8/4 10:27:00.
This article is licensed under a Creative Commons Attribution-NonCommercial 3.0 Unported Licence.

promising for detecting various, specific cell types. Conventional electrochemical methods have been used as immunosensors with low limits of detection.[30,84,85] However, traditional electrochemical methods are primarily indirect and based on sensing biomolecules eliminated from cells. In addition, these methods can rely on substrates with a high degree of functionalisation for cell or biomolecule-specific detection. Preparation of these substrates can be complex and time consuming, and might not be reusable. On the other hand, our system is capable of detecting the cells directly without needing additional functionalisation steps, reducing the complexity of our method. The components of our proposed setup can also be easily removed, sterilised and reused, greatly reducing the cost of our system for easy adoption.

Although impedance sampling can be performed on 3D scaffolds (tissues) or cells, sample preparation and measurement are more complex for tissue samples. Excised tissues are typically non-homogenous, containing various cell types with varying shapes, sizes and functions.[86,87] Moreover, the organisation and architecture of cells can vary between tissue samples, resulting in different measured outputs between each tissue slice or sample. Electrical characterisation is further complicated by the extracellular matrix that varies within tissue types.[87,88] As a result, performing electrical-based characterisation on a 2D cell monolayer can avoid the above complications. Furthermore, characterisations conducted in cells can be useful to understand the response of a single cell type, cell dynamics or cell-specific treatments.

On a cellular level, electrical characterisation can be performed for single-cells, cells in suspension and adhered cells in a monolayer. However, traditional methods of manipulating cells for single-cell measurements can be complex and cell-to-cell variations may result in inconsistency. Although results obtained from cells in suspension can be informative, it is difficult to translate the results to the tissue level as they cannot mimic the natural environment of tissues (*e.g.* cell–cell interactions, extracellular matrix *etc.*). Furthermore, cells in isolation do not respond as well to electric fields due to the lack of biochemical cues.[71,87,89] While a 2D cell monolayer lacks *in vivo* imitation, our method does not require complex sample preparation and can produce results within a shorter period of time.[86] Cell monolayers represent great potential for understanding the cell behaviour within a homogenous population, which can be valuable for clinical applications (*e.g.* cell-specific detection, drug testing). We present a few-step solution based on the combination of 2D MoS_2 and DC resistance to detect adherent cancer cells with a low limit of detection.

Conclusion

It has been challenging to detect an adherent monolayer of cells using electrical-based biosensors. Here, we demonstrate a sensitive detection method for a small adherent population of MCF-7 cells utilising an MoS_2-based DC resistance sensor. Atomistic MD simulations illustrate a decrease in Ψ_d due to MoS_2-facilitated lipid bilayer perturbation. Using our method, we were able to detect these micro-changes in the cell membrane with high sensitivity and low detection limit. Our proposed methodology represents a building block towards the development of clinically relevant lab-on-chip platforms. Nevertheless, further investigations for high throughput are needed for successful clinical and practical applications of the MoS_2-based electrical resistance sensor.

Conflicts of interest

The authors declare no competing interests.

Acknowledgements

We thank C. Cheung, K. G. Lim, L. T. Ng for important discussions. The authors acknowledge support from the Singapore University of Technology and Design (SUTDT12017003), Changi General Hospital (Singapore) (CGH-SUTD-HTIF2019-001), Ministry of Education (Singapore) (MOE2017-T2-2-064), SUTD-Zhejiang-University (SUTD-ZJU (VP) 201903) grant programs and Agency of Science, Technology and Research (Singapore) (A20G9b0135) grant programs. D. K. L. acknowledges support from the Massachusetts Institute of Technology–SUTD International Design Centre and National Supercomputing Centre, Singapore (15001618). S. S. Y. Chan acknowledges support from the SUTD President Graduate Scholarship.

References

1 T. Ji, Z. Liu, G. Q. Wang, X. Guo, S. Akbar khan, C. Lai, H. Chen, S. Huang, S. Xia, B. Chen, H. Jia, Y. Chen and Q. Zhou, *Biosens. Bioelectron.*, 2020, **166**, 112455.
2 National Cancer Institute, Cancer Statistics – National Cancer Institute, https://www.cancer.gov/about-cancer/understanding/statistics, accessed 3 May 2021.
3 A. Lim, *10 Important Cancer Statistics in Singapore (Updated 2021)*, https://smartwealth.sg/cancer-statistics-singapore/, accessed 28 June 2021.
4 L. M. Butler, Y. Perone, J. Dehairs, L. E. Lupien, V. de Laat, A. Talebi, M. Loda, W. B. Kinlaw and J. V. Swinnen, *Adv. Drug Delivery Rev.*, 2020, **159**, 245–293.
5 S. Zalba and T. L. M. ten Hagen, *Cancer Treat. Rev.*, 2017, **52**, 48–57.
6 T. Li, Q. Fan, T. Liu, X. Zhu, J. Zhao and G. Li, *Biosens. Bioelectron.*, 2010, **25**, 2686–2689.
7 H. A. Parsons, J. Rhoades, S. C. Reed, G. Gydush, P. Ram, P. Exman, K. Xiong, C. C. Lo, T. Li, M. Fleharty, G. J. Kirkner, D. Rotem, O. Cohen, F. Yu, M. Fitarelli-Kiehl, K. W. Leong, M. E. Hughes, S. M. Rosenberg, L. C. Collins, K. D. Miller, B. Blumenstiel, L. Trippa, C. Cibulskis, D. S. Neuberg, M. DeFelice, S. S. Freeman, N. J. Lennon, N. Wagle, G. Ha, D. G. Stover, A. D. Choudhury, G. Getz, E. P. Winer, M. Meyerson, N. U. Lin, I. Krop, J. C. Love, G. M. Makrigiorgos, A. H. Partridge, E. L. Mayer, T. R. Golub and V. A. Adalsteinsson, *Clin. Cancer Res.*, 2020, **26**, 2556–2564.
8 S. J. Singer and G. L. Nicolson, *Science*, 1972, **175**, 720–731.

Open Access Article. Published on 25 2021. Downloaded on 2025/8/4 10:27:00.
This article is licensed under a Creative Commons Attribution-NonCommercial 3.0 Unported Licence.

9 F. M. Goñi, *Biochim. Biophys. Acta, Biomembr.*, 2014, **1838**, 1467–1476.
10 M. R. Wenk, *Nat. Rev. Drug Discovery*, 2005, **4**, 594–610.
11 L. T.-H. Tan, K.-G. Chan, P. Pusparajah, W.-L. Lee, L.-H. Chuah, T. M. Khan, L.-H. Lee and B.-H. Goh, *Front. Pharmacol.*, 2017, **8**, 1–6.
12 G. L. Nicolson, *Biochim. Biophys. Acta, Biomembr.*, 2014, **1838**, 1451–1466.
13 G. Shahane, W. Ding, M. Palaiokostas and M. Orsi, *J. Mol. Model.*, 2019, **25**, 1–13.
14 T. Rivel, C. Ramseyer and S. Yesylevskyy, *Sci. Rep.*, 2019, **9**, 1–14.
15 A. A. Marino, I. G. Iliev, M. A. Schwalke, E. Gonzalez, K. C. Marler and C. A. Flanagan, *Tumor Biol.*, 1994, **15**, 82–89.
16 R. Latorre and J. E. Hall, *Nature*, 1976, **264**, 361–363.
17 M. Yang and W. J. Brackenbury, *Front. Physiol.*, 2013, **4**, 185.
18 T. Starke-Peterkovic, N. Turner, P. L. Else and R. J. Clarke, *Am. J. Physiol.: Regul., Integr. Comp. Physiol.*, 2005, **288**, R663–R670.
19 S. Eissa, R. Chinnappan and M. Zourob, *Electroanalysis*, 2017, **29**, 1994–2000.
20 Y. Chen, J. Peng, Y. Lai, B. Wu, L. Sun and J. Weng, *Biosens. Bioelectron.*, 2019, **142**, 111520.
21 H. Brockman, *Chem. Phys. Lipids*, 1994, **73**, 57–79.
22 L. Wang, *Annu. Rev. Biochem.*, 2012, **81**, 615–635.
23 R. F. Flewelling and W. L. Hubbel, *Biophys. J.*, 1996, **49**, 541–552.
24 R. A. Pearlstein, C. J. Dickson and V. Hornak, *Biochim. Biophys. Acta, Biomembr.*, 2017, **1859**, 177–194.
25 W. Ding, M. Palaiokostas, W. Wang and M. Orsi, *J. Phys. Chem. B*, 2015, **119**, 15263–15274.
26 M. Jan Akhunzada, F. D'Autilia, B. Chandramouli, N. Bhattacharjee, A. Catte, R. Di Rienzo, F. Cardarelli and G. Brancato, *Sci. Rep.*, 2019, **9**, 1–12.
27 Y. Furukawa, A. Shimada, K. Kato, H. Iwata and K. Torimitsu, *Biochim. Biophys. Acta, Gen. Subj.*, 2013, **1830**, 4329–4333.
28 S. K. Rastogi, J. Bliley, D. J. Shiwarski, G. Raghavan, A. W. Feinberg and T. Cohen-Karni, *Cell. Mol. Bioeng.*, 2018, **11**, 407–418.
29 M. Mayer, O. Arrizabalaga, F. Lieb, M. Ciba, S. Ritter and C. Thielemann, *Biosens. Bioelectron.*, 2018, **100**, 462–468.
30 D. K. Loke, G. J. Clausen, J. F. Ohmura, T. C. Chong and A. M. Belcher, *ACS Appl. Nano Mater.*, 2018, **1**, 6556–6562.
31 L. Li, A. M. Belcher and D. K. Loke, *Nanoscale*, 2020, **12**, 24214–24227.
32 L. Feng, Y. Chen, J. Ren and X. Qu, *Biomaterials*, 2011, **32**, 2930–2937.
33 Y. Song, Y. Chen, L. Feng, J. Ren and X. Qu, *Chem. Commun.*, 2011, **47**, 4436–4438; *Chem*, 2020, **311**, 127863.
34 Y. Shu, L. Zhang, H. Cai, Y. Yang, J. Zeng, D. Ma and Q. Gao, *Sens. Actuators, B*, 2020, **311**, 127863.
35 X. Qian, S. Shen, T. Liu, L. Cheng and Z. Liu, *Nanoscale*, 2015, **7**, 6380–6387.
36 H. J. Yoon, T. H. Kim, Z. Zhang, E. Azizi, T. M. Pham, C. Paoletti, J. Lin, N. Ramnath, M. S. Wicha, D. F. Hayes, D. M. Simeone and S. Nagrath, *Nat. Nanotechnol.*, 2013, **8**, 735–741.
37 L. Cheng, X. Wang, F. Gong, T. Liu and Z. Liu, *Adv. Mater.*, 2020, **32**, 1902333.
38 M. Xu, T. Liang, M. Shi and H. Chen, *Chem. Rev.*, 2013, **113**, 3766–3798.
39 M. Chhowalla, Z. Liu and H. Zhang, *Chem. Soc. Rev.*, 2015, **44**, 2584–2586.
40 J. H. Appel, D. O. Li, J. D. Podlevsky, A. Debnath, A. A. Green, Q. H. Wang and J. Chae, *ACS Biomater. Sci. Eng.*, 2016, **2**, 361–367.
41 S. S. Chan, Y. S. Tan, K. X. Wu, C. Cheung and D. K. Loke, *ACS Appl. Bio Mater.*, 2018, **1**, 210–215.
42 X. Zhu, X. Ji, N. Kong, Y. Chen, M. Mahmoundi, X. Xu, L. Ding, W. Tao, T. Cai, Y. Li, T. Gan, A. Barret, Z. Bharwani, H. Chen and O. C. Farokhzad, *ACS Nano*, 2018, **12**, 2922–2938.
43 S. Cai, J. Yan, H. Xiong, Q. Wu, H. Xing, Y. Liu, S. Liu and Z. Liu, *Int. J. Pharm.*, 2020, **590**, 119948.
44 T. Liu, C. Wang, W. Cui, H. Gong, C. Liang, X. Shi, Z. Li, B. Sun and Z. Liu, *Nanoscale*, 2014, **6**, 11219–11225.
45 B. Pang, H. Yang, L. Wang, J. Chen, L. Jin and B. Shen, *Colloids Surf., A*, 2021, **608**, 125506.
46 S. Wang, J. Qiu, W. Guo, X. Yu, J. Nie, J. Zhang, X. Zhang, Z. Liu, X. Mou, L. Li and H. Liu, *Adv. Biosyst.*, 2017, **1**, 1–9.
47 H. Nazari, A. Heirani-Tabasi, M. S. Alavijeh, Z. S. Jeshvaghani, E. Esmaeili, S. Hosseinzadeh, F. Mohabatpour, B. Taheri, S. H. A. Tafti and M. Soleimani, *ChemistrySelect*, 2019, **4**, 11557–11563.
48 J. Lee, P. Dak, Y. Lee, H. Park, W. Choi, M. A. Alam and S. Kim, *Sci. Rep.*, 2014, **4**, 1–7.
49 A. Kálosi, M. Labudová, A. Annušová, M. Benkovičová, M. Bodík, J. Kollár, M. Kotlár, P. Kasak, M. Jergel, S. Pastoreková, P. Siffalovic and E. Majkova, *Biomater. Sci.*, 2020, **8**, 1973–1980.
50 S. S. Y. Chan, Y. S. Tan, K.-X. Wu, C. Cheung and D. K. Loke, *ACS Appl. Bio Mater.*, 2018, **1**, 210–215.
51 V. Varshney, S. S. Patnaik, C. Muratore, A. K. Roy, A. A. Voevodin and B. L. Farmer, *Comput. Mater. Sci.*, 2010, **48**, 101–108.
52 B. Luan and R. Zhou, *Appl. Phys. Lett.*, 2016, **108**, 1–5.
53 S. Jo, T. Kim, V. G. Iyer and W. Im, *J. Comput. Chem.*, 2008, **29**, 1859–1865.
54 S. Jo, J. B. Lim, J. B. Klauda and W. Im, *Biophys. J.*, 2009, **97**, 50–58.
55 J. P. M. Jämbeck and A. P. Lyubartsev, *J. Chem. Theory Comput.*, 2012, **8**, 2938–2948.
56 J. P. M. Jämbeck and A. P. Lyubartsev, *J. Phys. Chem. B*, 2012, **116**, 3164–3179.
57 M. J. Abraham, T. Murtola, R. Schulz, S. Páll, J. C. Smith, B. Hess and E. Lindah, *SoftwareX*, 2015, **1–2**, 19–25.
58 W. L. Jorgensen, J. Chandrasekhar, J. D. Madura, R. W. Impey and M. L. Klein, *J. Chem. Phys.*, 1983, **79**, 926–935.
59 G. Bussi, D. Donadio and M. Parrinello, *J. Chem. Phys.*, 2007, **126**, 014101.

 © 2021 The Author(s). Published by the Royal Society of Chemistry

Open Access Article. Published on 25 2021. Downloaded on 2025/8/4 10:27:00.
This article is licensed under a Creative Commons Attribution-NonCommercial 3.0 Unported Licence.

60 M. Parrinello and A. Rahman, *J. Appl. Phys.*, 1981, **52**, 7182–7190.
61 W. G. Hoover, *Phys. Rev. A: At., Mol., Opt. Phys.*, 1985, **31**, 1695–1697.
62 S. Nosé, *J. Chem. Phys.*, 1984, **81**, 511–519.
63 T. Darden, D. York and L. Pedersen, *J. Chem. Phys.*, 1993, **98**, 10089–10092.
64 U. Essmann, L. Perera, M. L. Berkowitz, T. Darden, H. Lee and L. G. Pedersen, *J. Chem. Phys.*, 1995, **103**, 8577–8593.
65 M. Klähn and M. Zacharias, *Phys. Chem. Chem. Phys.*, 2013, **15**, 14427–14441.
66 S. Das and J. Appenzeller, *Nano Lett.*, 2013, **13**, 3396–3402.
67 J. Na, M. Shin, M. K. Joo, J. Huh, Y. Jeong Kim, H. Jong Choi, J. Hyung Shim and G. T. Kim, *Appl. Phys. Lett.*, 2014, **104**, 233502.
68 S. Das and J. Appenzeller, *Phys. Status Solidi RRL*, 2013, **7**, 268–273.
69 L. Liang and V. Meunier, *Nanoscale*, 2014, **6**, 5394–5401.
70 P. Shah, T. N. Narayanan, C. Z. Li and S. Alwarappan, *Nanotechnology*, 2015, **26**, 1–7.
71 P. Shah, X. Zhu, X. Zhang, J. He and C. Z. Li, *ACS Appl. Mater. Interfaces*, 2016, **8**, 5804–5812.
72 Y. An, T. Jin, F. Zhang and P. He, *J. Electroanal. Chem.*, 2019, **834**, 180–186.
73 L. Wang, J. Zhu, C. Deng, W. L. Xing and J. Cheng, *Lab Chip*, 2008, **8**, 872–878.
74 H. Wang, H. Li, Y. Huang, M. Xiong, F. Wang and C. Li, *Biosens. Bioelectron.*, 2019, **142**, 111531.
75 J. Liu, Y. Qin, D. Li, T. Wang, Y. Liu, J. Wang and E. Wang, *Biosens. Bioelectron.*, 2013, **41**, 436–441.
76 I. R. Suhito, N. Angeline, S. S. Choo, H. Y. Woo, T. Paik, T. Lee and T. H. Kim, *Sensors*, 2018, **18**, 1–17.
77 J. Zhang, J. Shi, W. Liu, K. Zhang, H. Zhao, H. Zhang and Z. Zhang, *Sens. Actuators, B*, 2018, **276**, 552–559.
78 D. Yang, M. Liu, J. Xu, C. Yang, X. Wang, Y. Lou, N. He and Z. Wang, *Talanta*, 2018, **185**, 113–117.
79 Z. Liao, L. Han, Q. Li, L. Li, Y. Liu, Y. Song, W. Tan and E. Song, *Adv. Funct. Mater.*, 2021, **31**, 1–11.
80 C. H. Yea, H. C. Jeong, S. H. Moon, M. O. Lee, K. J. Kim, J. W. Choi and H. J. Cha, *Biomaterials*, 2016, **75**, 250–259.
81 H. C. Jeong, S. S. Choo, K. T. Kim, K. S. Hong, S. H. Moon, H. J. Cha and T. H. Kim, *Sens. Actuators, B*, 2017, **242**, 224–230.
82 I. R. Suhito, E. S. Kang, D. S. Kim, S. Baek, S. J. Park, S. H. Moon, Z. Luo, D. Lee, J. Min and T. H. Kim, *Colloids Surf., B*, 2019, **180**, 384–392.
83 N. Angeline, S. S. Choo, C. H. Kim, S. H. Bhang and T. H. Kim, *BioChip J.*, 2021, **15**, 52–60.
84 Q. Guo, X. Li, C. Shen, S. Zhang, H. Qi, T. Li and M. Yang, *Microchim. Acta*, 2015, **182**, 1483–1489.
85 A. A. M. Abdurhman, Y. Zhang, G. Zhang and S. Wang, *Anal. Bioanal. Chem.*, 2015, **407**, 8129–8136.
86 M. Kapałczyńska, T. Kolenda, W. Przybyła, M. Zajączkowska, A. Teresiak, V. Filas, M. Ibbs, R. Bliźniak, Ł. Łuczewski and K. Lamperska, *Arch. Med. Sci.*, 2018, **14**, 910–919.
87 M. J. Peters, J. G. Stinstra and I. Leveles, in *Modeling and Imaging of Bioelectrical Activity*, 2004, pp. 281–319.
88 H. P. Schwan, *Adv. Biol. Med. Phys.*, 1957, **5**, 147–209.
89 K. Zhu, N. R. Hum, B. Reid, Q. Sun, G. G. Loots and M. Zhao, *Sci. Rep.*, 2020, **10**, 1–11.